Supporting Information

Liquid Processing of Interfacially Grown Iron-Oxide Flowers into 2D-Platelets yields Lithium-ion Battery Anodes with Capacities of Twice the Theoretical Value

Bharathi Konkena[1], Harneet Kaur[1§], Ruiyuan Tian[1§], Cian Gabbett[1], Mark McCrystall[1], Dominik Valter Horvath[1], Kevin Synnatschke[1], Ahin Roy[2], Ross Smith[2], Valeria Nicolosi[2], Micheál D. Scanlon[3]*, and Jonathan N. Coleman[1]*

§Authors contributed equally to this work

[1]School of Physics, CRANN & AMBER Research Centres, Trinity College Dublin, Dublin 2, Ireland.

[2]School of Chemistry, CRANN & AMBER Research Centres, Trinity College Dublin, Dublin 2, Ireland.

[3] The Bernal Institute and Department of Chemical Sciences, University of Limerick, Limerick V94 T9PX, Ireland.

Email: *colemaj@tcd.ie (Jonathan N. Coleman);

*micheal.scanlon@ul.ie (Micheál D. Scanlon)

S1: Synthesis of iron oxide nanstructures at liquid-liquid interface

Interfaces between two immiscible electrolyte solutions (ITIES) can be polarized either by using a potentiostat externally (electrodes) or chemically by changing the composition or concentration of supporting electrolytes (common ions) in the organic or aqueous phase. Our approach herein is the use of ClO_4^- as a common ion which induces the specific potential difference across the interface according to the Nernst–Donnan equations. Here, electrodeless polarization of the ITIES is achieved through distribution of perchlorate anions ClO_4^- between the phases, inducing a specific Galvani potential difference ($\Delta_o^w\phi$) negative of the open circuit potential (OCP) across the water/DCE interface (Figure S1).

In order to elucidate the effect of the ClO_4^- ion polarization, identical experiments were performed without electrifying the interface (without ClO_4^- ion). A completely different "nanoparticle" morphology was observed for the biphasic cell without ClO_4^- ion polarisation (Figure S2). Furthermore, a different needle type FeOOH structure was observed with a very low 4-aminopyridine concentration (typically less than 1 mM) at a ClO_4^- ion polarized interface (Figure S2). This indicates that the ClO_4^- ion plays a crucial role in directing the 2D-sheet like morphology of Fe_2O_3 and TBA^+ may act as a structure directing reagent to take control over the morphology to lead a transition from 2D to 3D flower-like architectures.

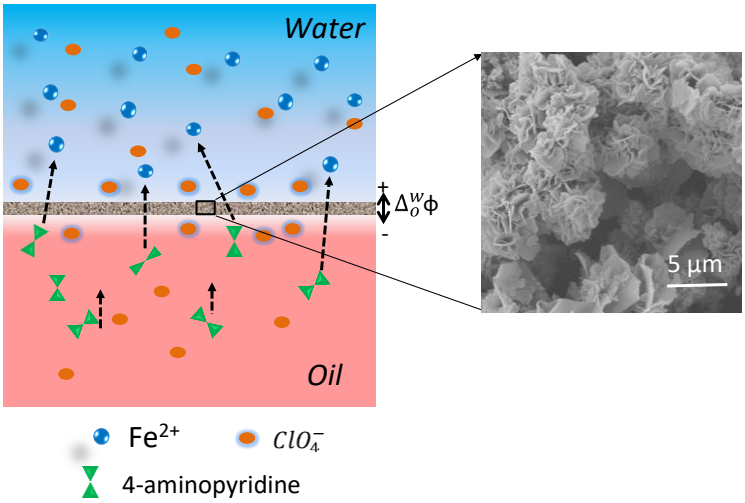

Figure S1. Schematic representation of the interface for the polarization of ITIES. The Fe_2O_3 microstructures assembled at the water/DCE interface. The interface is electrified/polarized by distribution of the common ion, ClO_4^-, that partitions between the two liquid phases.

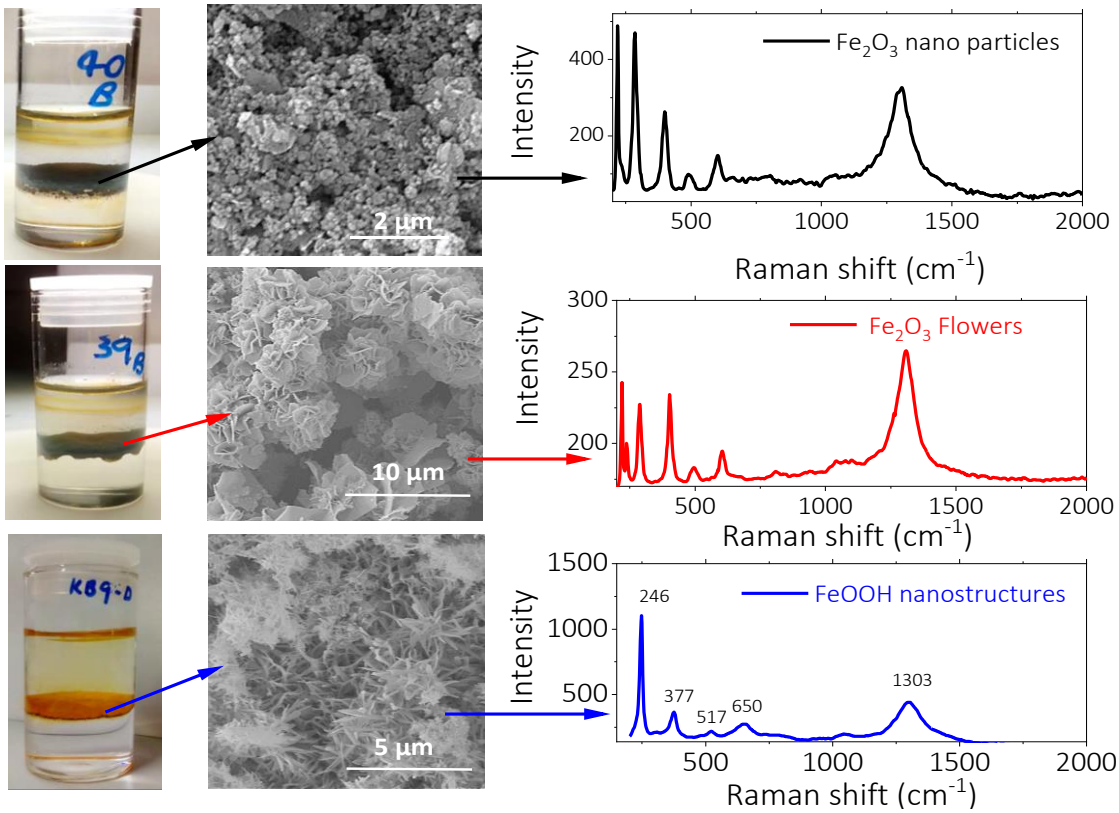

Figure S2. Synthesis iron oxide nanostructures with and without electrifying the L/L interface. SEM images and Raman spectra of as synthesized powders.

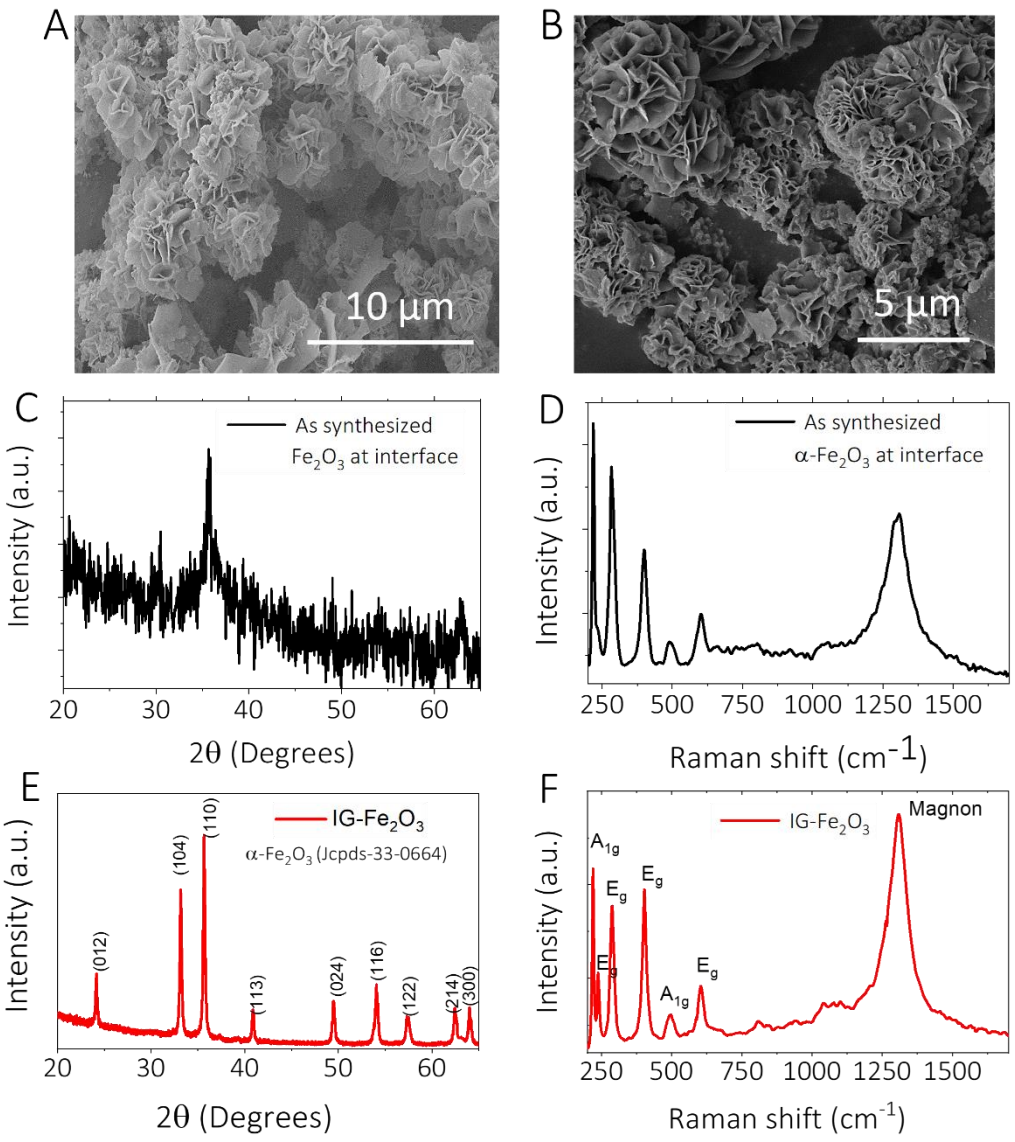

Figure S3. Structural characterization of interfacial grown α-Fe_2O_3 flowers before and after annealing. SEM image of interfacial grown α-Fe_2O_3 powder sample (A) before and (B) after annealing at 350ºC for 3 hours. It is worth noting that the surface morphology of the samples after heat-treatment at 350ºC are similar to that of as prepared sample. XRD pattern of the interfacial grown α-Fe_2O_3 powder (C) before and (E) after annealing. High intense peaks were observed after heat treatment suggesting high crystallinity of the sample. Raman scattering spectrum of interfacial grown α-Fe_2O_3 powder (D) before and (F) after annealing are very similar.

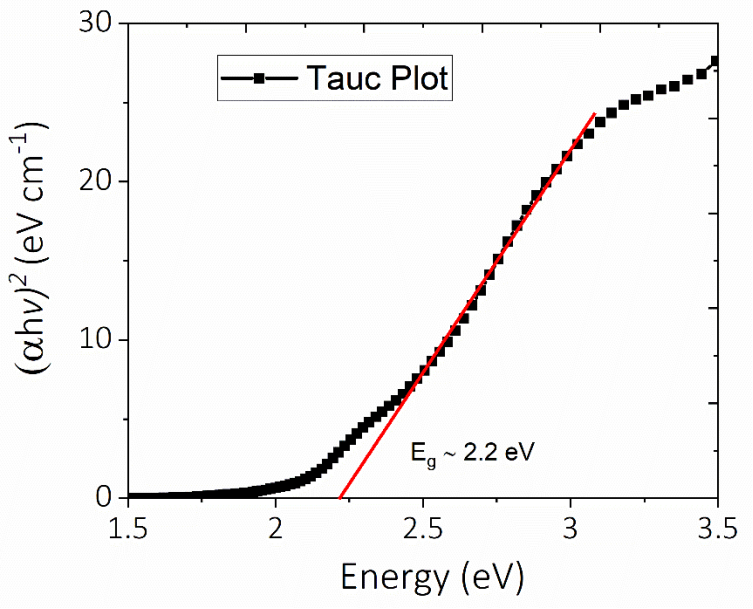

Figure S4. The bandgap of the 2D flakes is determined from the Tauc plot. For a direct bandgap material like Fe_2O_3, the square of the product of the absorption coefficient (α) and photon energy ($h\nu$) is plotted *versus* the photon energy. The Band gap is obtained by extrapolating the last linear segment of the plot. The estimate the optical band gap (Eg) for exfoliated 2D flakes is found to be 2.2 eV.

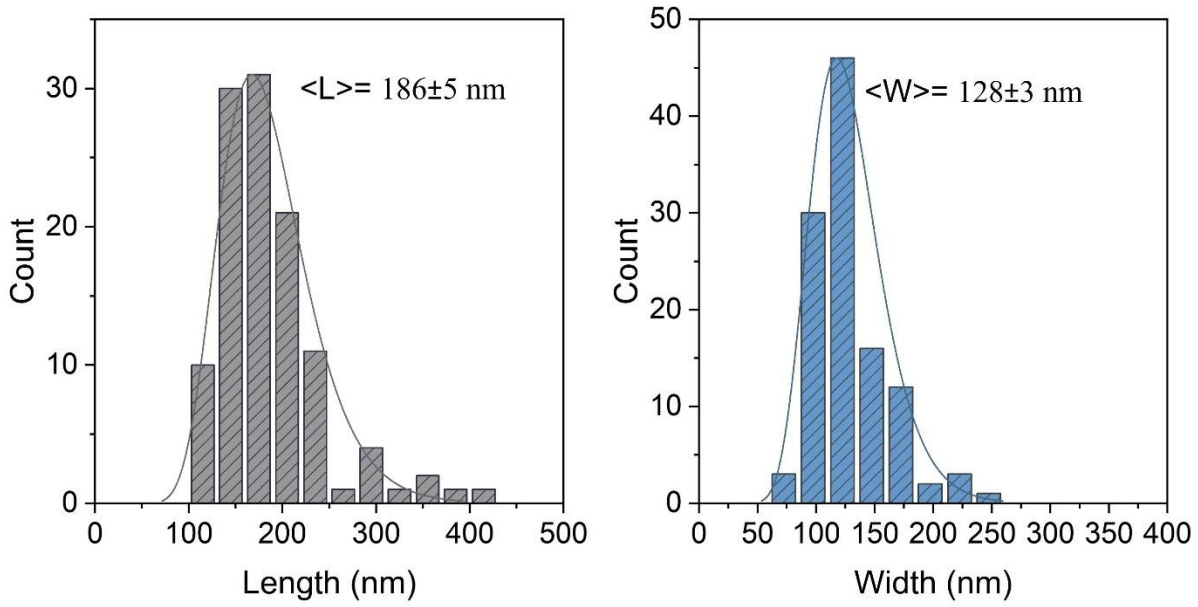

Figure S5. Length and width histogram from TEM analysis.

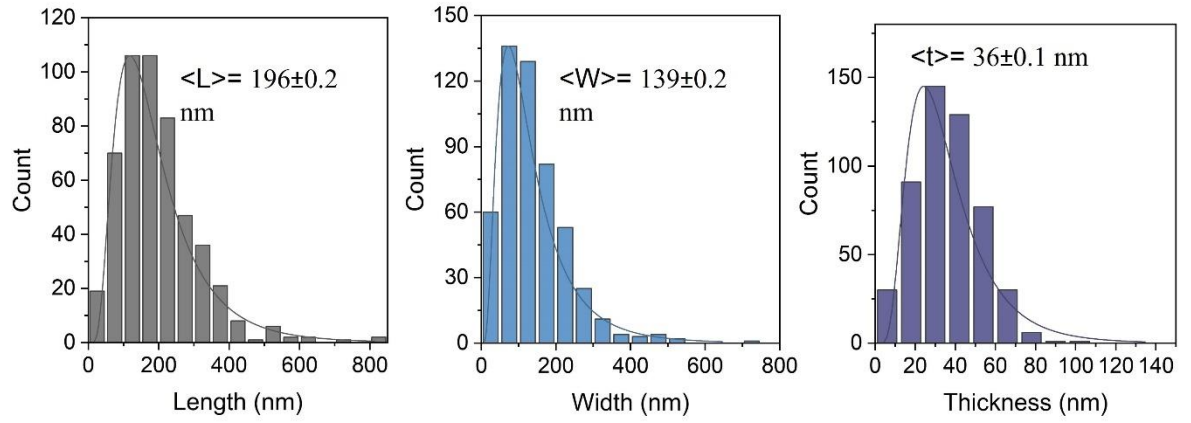

Figure S6. Statistical distribution of length, width and thickness variation of the 2D-platelets by AFM.

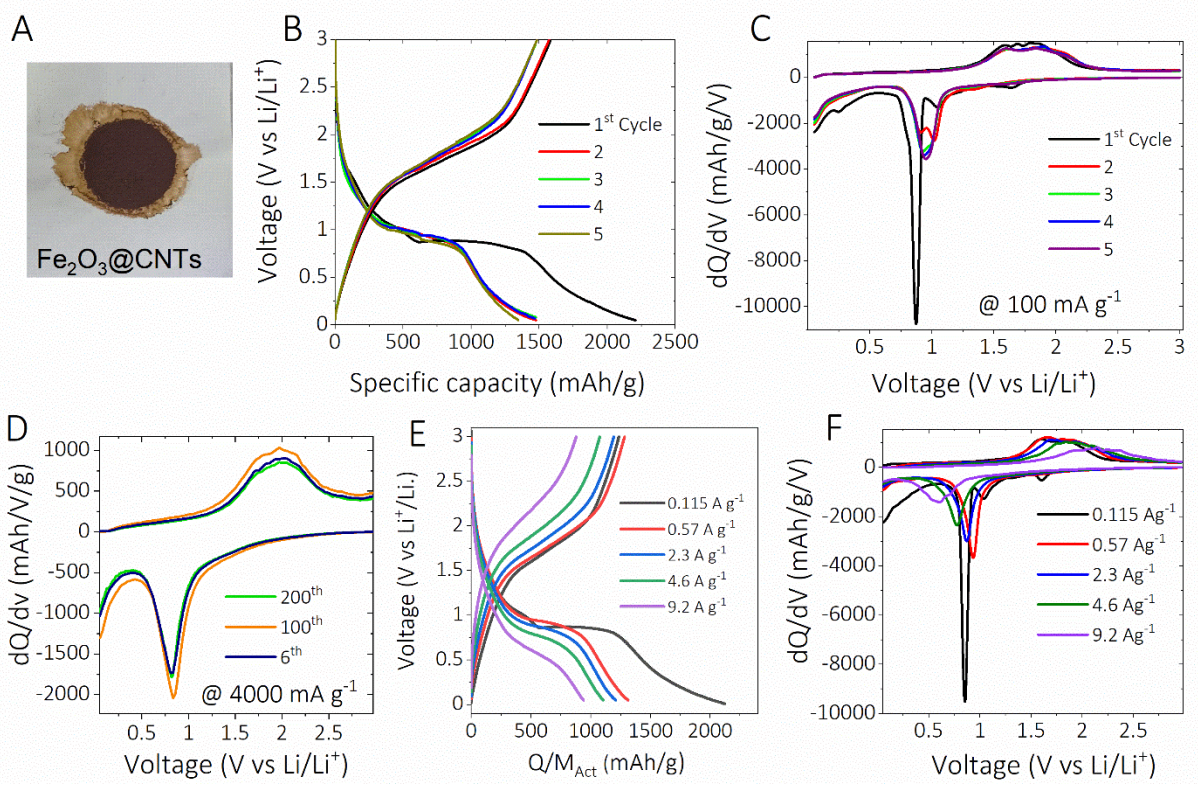

Figure S7. Charge-discharge curves and corresponding dQ/dv profiles. (A) Vacuum filtered film of the α-Fe_2O_3/CNTs composite. (B) Charge-discharge profiles of α-Fe_2O_3/CNTs electrodes for the first five cycles at 100 mA g^{-1}. (C) dQ/dv profiles of α-Fe_2O_3/CNTs electrodes for the first cycle at 100 mA g^{-1}. (D) dQ/dv profiles for the 6, 100 and 200 cycles at 4000 mA g^{-1}. (E) Charge-discharge profile of the of α-Fe_2O_3/CNTs electrodes at different rates (relevant to Figure 4F shown in the main draft). (F) Corresponding dQ/dv profile at different rates.

The lithiation process of α-Fe_2O_3 electrodes can be described into three regions:[1-3] (i) intercalation region where random intercalation of Li^+ into α-Fe_2O_3 the takes place (3.0–1.5 V); (ii) main conversion region where the reduction of α-Fe_2O_3 into Fe^0 takes place (1.5–0.6 V); (iii) extra capacity region (0.6–0.001 V), where the reversible electrolyte decomposition occurs.[3, 4] For α-Fe_2O_3/CNTs electrodes, these three regions are observed with an identification of intense peak centred at 0.92 V of the conversion region (ii). Clearly, the dQ/dv profiles for the first 5 cycles at 100 mA g^{-1} as shown in Figure S8B also match well with the similar lithium-storage mechanisms in the three reactions from Eq. (1) to eq.(3)). Notably, during the lithiation process the conversion reaction is mainly limited by the lithium diffusion into the Li_2O layers rather than charge transfer at fast rates. Graphically, this limitation is evidenced by the peak intensity reduction (suggesting a less reacting active material) and peak shift toward the lower voltage region (suggesting the rise of polarization) as shown in Figure S8 F.

S2: Extended activation processes at 4000 or 7000 mA g^{-1}

For the extended activation process, the Fe_2O_3/CNTs electrodes were cycled at 100 mA g^{-1} for 5 cycles followed by 25 cycles at higher currents (4000 mA g^{-1} or 7000 mA g^{-1}) for 5 repetitive times (indicates activation), followed by a rate performance at various current rates for 10 cycles (indicates rate capability), later remain continued cycling at 7000 mA g^{-1} for 120 cycles (indicates stability) and finally the current density switching back to low rate (100 mA g^{-1}) for 10 cycles to check the electrode at the end.

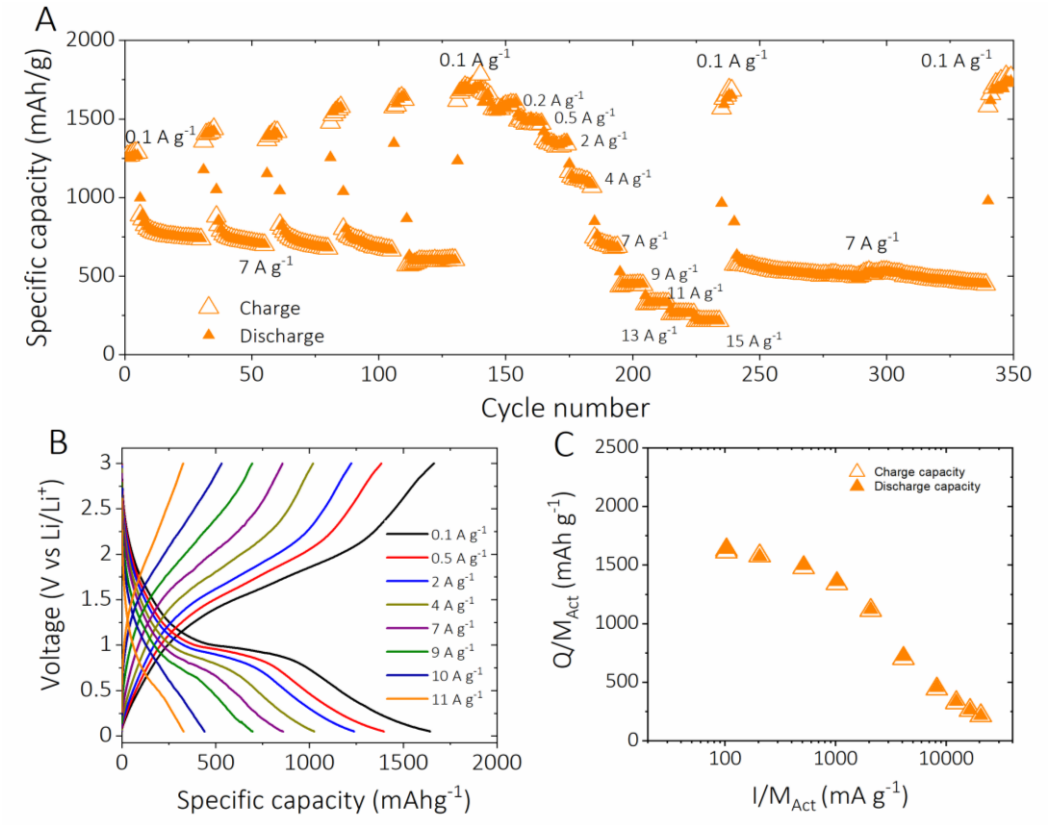

Figure S8. (A) Galvanostatic charge-discharge cycling performance of the α-Fe_2O_3/nanotube composite electrode with an extended activation processes at two different current densities 100 mA g^{-1} and 7000 mA g^{-1}. In all cases, capacity and current are normalised to the active mass of the α-Fe_2O_3. (F) Charge-discharge curves measured after extended activation at 7000 mA g^{-1} at different specific currents for α-Fe_2O_3/nanotube composite anodes. (C) Rate capability plotted as specific capacity versus current data obtained after extended activation 140 cycles at 7000 mA g^{-1}.

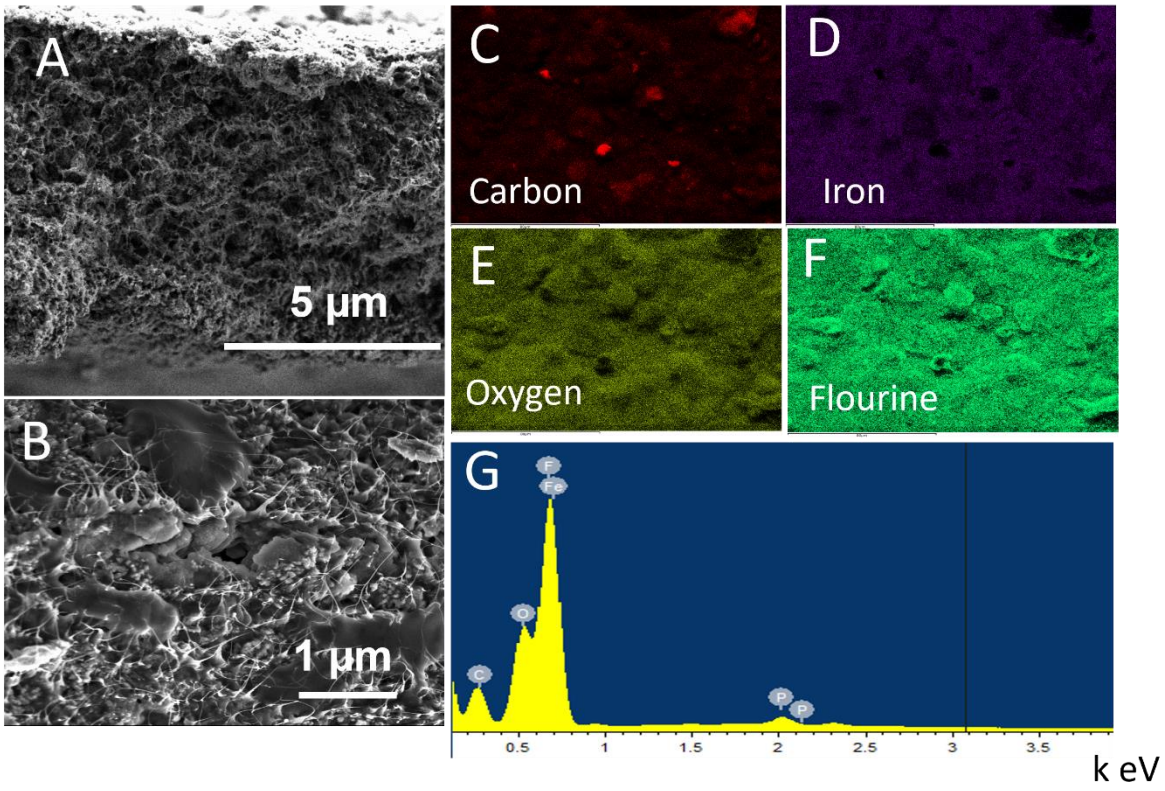

Figure S9. (A) SEM images of the α-Fe_2O_3/nanotube composite electrode before activation and (B) after the activation processes of 145 cycles. The elemental mapping on the activated electrode surface, for (C) Carbon; (D) Iron; (E) oxygen; and (F) fluorine form the electrolyte. (G) EDX spectra on the post activated electrode.

S3: dQ/dv plots during the course of extended activation processes at 4000 mA g^{-1}

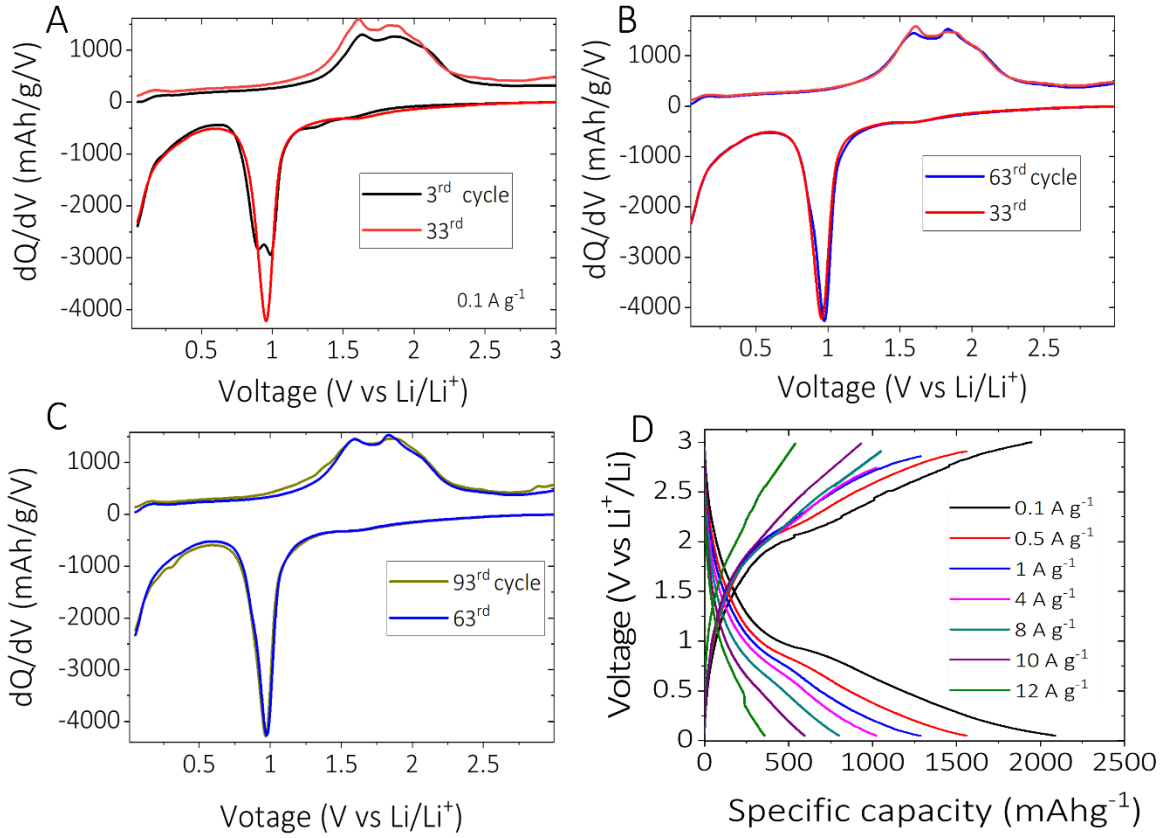

Figure S10. (A-C) Comparison of dQ/dv profiles of α-Fe_2O_3/CNTs electrodes during the course of the activation for the selected cycles at 3, 33,63, and 93 at current density of 100 mA g^{-1}. (D) dQ/dv profiles for the 6, 100 and 200 cycles at 4000 mA g^{-1}. (D) Charge-discharge curves measured after activation of 145 cycles (for data shown in the Figure 5A) at different specific currents for α-Fe_2O_3/CNT composite anodes.

S4: Electrochemical impedance spectra (EIS)

To clarify the electrochemical performance of the α-Fe_2O_3/CNTs composite electrodes, we further performed the impedance spectra along the course of activation process. Upon being discharged to a selected state, i.e., at 5th (1000 mA g^{-1}), 125th (4000 mA g^{-1}), and 145th (100 mA g^{-1}) cycles, a spectrum was acquired after the cell was allowed to equilibrate for 0.5 h. The spectrum shows a depressed semicircle followed by an inclined line in Figure S12. Nyquist plot can be simulated by a circuit consisting of an electrolyte resistance (R_0) in series with a Randles-type impedance element and with an extra blocking CPE2 (constant phase element), as shown Figure S12, and values are listed in Table in Figure S12. The CPE2, rather than ideal capacitor, has been introduced in order to simulate the depressed nature of the intermediate frequency semicircle and the nonideality of the blocking capacitance at the low-frequency end. One possible origin for such CPE2 characteristics might arise from the porous nature of the electrode.[5, 6] It is also evidenced by the strengthened capacitive-like behaviour by the steeper increase of the Z'-Z″ curves at low frequencies. The decrease in charge transfer resistance of electrodes was also observed after activation, suggesting the dominance of charge transfer interfacial interactions over diffusion-controlled ones.

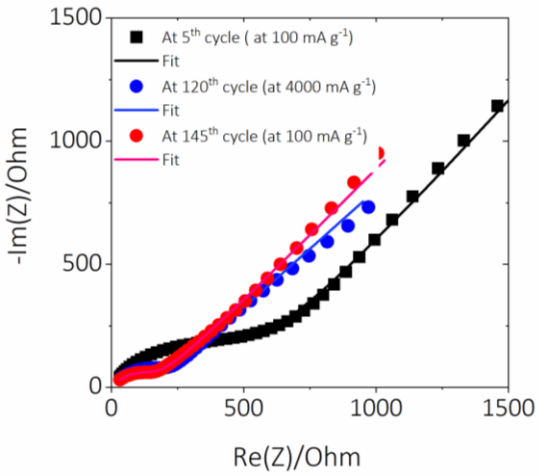

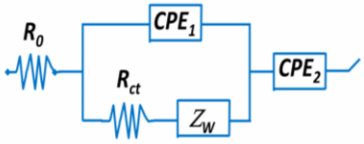

	R_{Sol}	R_{ct}	CPE_1	CPE_2
5th Cycle (at 0.1 Ag^{-1})	0.5 Ω	545 Ω	6.3 x 10^{-6} *F*	30.6 *F*
120th Cycles (at 4 Ag^{-1})	8.8 Ω	157 Ω	7.8 x 10^{-6} *F*	35.3 *F*
145th Cycle (at 0.1 Ag^{-1})	7.9 Ω	163 Ω	9.5 x 10^{-6} *F*	0.012 *F*

Figure S12. The Nyquist plot and Randles-type equivalent circuit for α-Fe_2O_3/CNT electrodes at selected cycles at 100 mA g^{-1} (black); at 4000 mA g^{-1} (blue); when switched back to 100 mA g^{-1} (red).

S5: Diffusion Constant (D)

To calculate the chemical diffusion coefficient for Li^+ in the α-Fe_2O_3 particles, we used the Randles-sevcik equation:

$$i_p = 2.69 \times 10^5 \, n^{3/2} \, A \, C \, D^{1/2} v^{1/2} \quad \text{(S1)}$$

i_p = peak current (A)

D = chemical diffusion constant for the Li^+ ions in $cm^2 \, s^{-1}$

ν = scan rate ($V. \, s^{-1}$)

n = number of charge transfer

A = geometric area of the electrode (cm^2)

C = concentration of lithium ($mol. \, cm^{-3}$)

To calculate D_{Li+} more quantitatively, we note that, because of the dependence of i on both ν and $ν^{1/2}$ for our Fe_2O_3/CNT electrodes data, a better parameter to consider k_2 value obtained from equation $ip = k_1 ν + k_2 ν^{1/2}$ to fit into Randles-sevcik equation.

S6: Density of the electrodes

The density (ρ) of the electrode (g/cm^3) can be calculated using equation:

$$\rho = \frac{m}{A \times L_E} \quad \text{(S2)}$$

where *m* is the mass of the α-Fe_2O_3/CNT composite electrode (g), *A* is the area of the electrode (0.178 cm^2), L_E is the average thickness of the α-Fe_2O_3/CNT composite electrode. The thickness of the electrode was estimated from the cross-section FESEM images shown in Figure 5B in the main draft. The average thickness of the α-Fe_2O_3/CNT composite electrodes is measured to be ~5.9 μm before activation and 8.8 μm after activation.

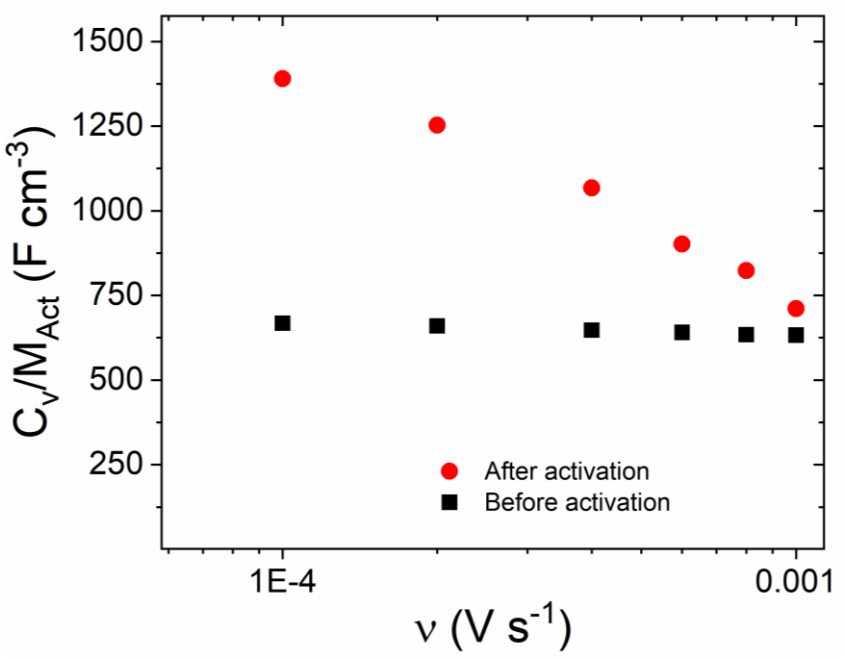

Figure S13. Volumetric capacitance (C_V) of the α-Fe_2O_3/CNT composite electrodes as a function of scan rate ranging from 0.1−1 mV s^{-1}.

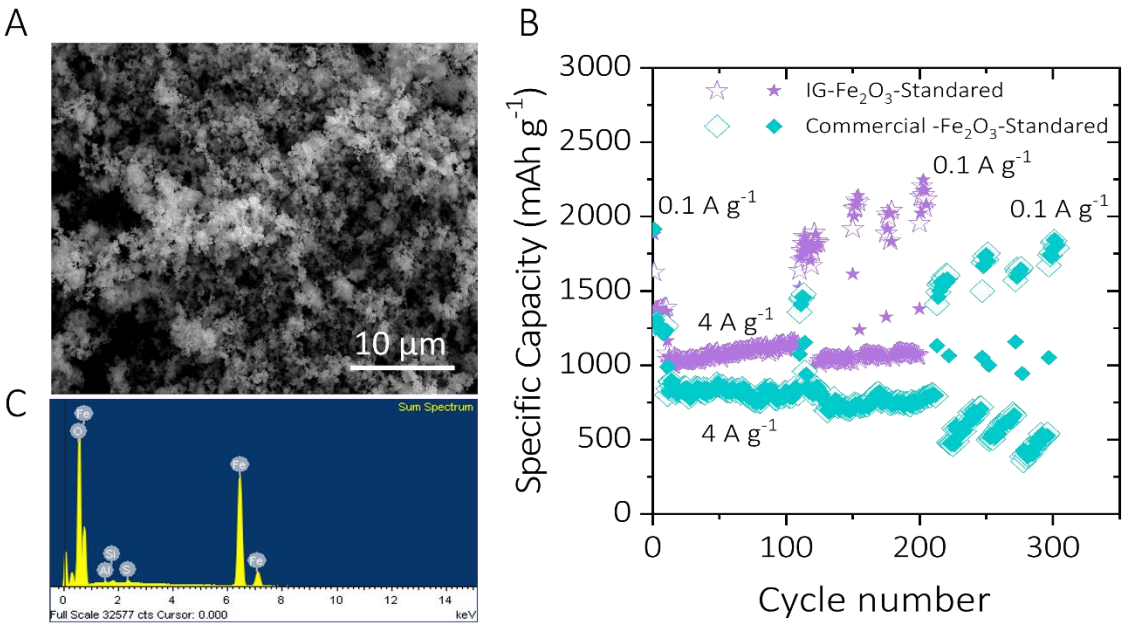

Figure S14. Comparison of commercial versus IG-Fe_2O_3. (A) SEM image of filtered commercial exfoliated standard dispersion. The commercial α-Fe_2O_3 was exfoliated as same as described for IG-α-Fe_2O_3 and percolated with CNT (30 %) and evaluated the electrochemical performance of both composite electrodes, (M_f^{CNTs} = 30%, A = 0.178 cm^2, M_T/A = 0.67 mg cm^{-2}). Activation cycling performance for both α-Fe_2O_3/CNT composite anodes cycled at 100 mA g^{-1} for first five cycles and 4000 mA g^{-1} with four repetitive times.

To better understand the shape effect, we exfoliated the commercial Fe_2O_3 and percolated with CNT (30 %) and evaluated the electrochemical performance of the composite electrode. As shown in Figure S14, interfacial grown (IG) Fe_2O_3/CNT electrodes display the more reversible capacity of 1160 mAh g^{-1} at 4000 mAg^{-1} and dramatically improved and reaching to 2200 mAh g^{-1} at 100 mA g^{-1} after 200 cycles. While, exfoliated commercial Fe_2O_3/CNT electrodes delivers little lower reversible capacity of 850 mAh g^{-1} at 4000 mA g^{-1} and gradually increased to 1843 mAh g^{-1} at 100 mA g^{-1} after 300 cycles. Both the Li^+ diffusion and electron transport kinetics within the commercial Fe_2O_3 nanoparticles are sluggish. On the other hand, IG-Fe_2O_3 quasi 2D-flakes increasing the chance of full contact with SWCNTs by exposing thinner sheets to the conductive network, leading to much enhanced utilization of Fe_2O_3 and improved capacity and cycling, as shown in Figure S14.

Table S1: Li-storage capacities reported in the literature for Fe_2O_3/CNTs based composite anodes at various current densities.

Ref.	Anode Material	C-content (%)	Initial capacity (mA h g^{-1})	Reversible capacity (mA h g^{-1})	Current rate (mA g^{-1})
7	Fe_2O_3 coated CNT	55 %	1144	963	50
8	Fe_2O_3 filled CNT	80 %	1092	867	50
9	Fe_2O_3/SWCNT	30 %	692	1007	200
10	Fe_2O_3/C/CNT	72 %	1390	1230	100
11	CNT/Fe_2O_3/C	-	1773	1213	100
12	CNT/γFe_2O_3/C	-	981	919	100
13	α-Fe_2O_3 nanohorns / CNTs	70	1060	820	500
14	Core–shell α-Fe_2O_3 / CNTs	20 %	1290	1173	200
15	α-Fe_2O_3 nanorods/CNTs–G	-	1310	1000	200
		-	1692	1118	100
16	3D rGO/MWCNTs /α-Fe_2O_3	30 %	1000	690	40
17	α-Fe_2O_3 nanosphere/CNT	-	1200	870	100
18	α-Fe_2O_3 NPs/SWCNT	-	1950	1200	500
19	α-Fe_2O_3 nanoplates	42 %	1200	712	400
20	Fe_2O_3/COOH-MWCNT	50 %	1200	860	500
	γ-Fe_2O_3@CNTs	-	1100	623	50
21	α Fe_2O_3 NPs/CNTS	60 %	2081	768	35
22	α & γ - Fe_2O_3 filled CNTS	70 %	870	515	100
23	α Fe_2O_3/MWCNTS	48 %	1192	866	100
24		85 %	1000	488	50

[25]	α Fe_2O_3 nanobelts/CNTS	38 %	1278	960	200
[26]	α Fe_2O_3-CNFs	-	1214	820	100
[27]	α Fe_2O_3nanorods-CNFs	25%	1278	960	200
[28]	α Fe_2O_3/CNFs	-	844	292	12000
[29]	Fe_2O_3/rGO/CNFs		1250	811	100
This work	**α-Fe_2O_3 / CNTs**	30 %	1584	1500	100
				1168	4000
				730	7000
				530	12000
				2113	100

Modelling rate performance

The characteristic time associated with charge / discharge, τ, is given by an equation[30] which can be rewritten slightly to highlight the fact that it can be separated into capacitive and diffusive terms.

$$\tau = \tau_C + \tau_D =$$

$$\tau = 28Q_V\left[\frac{L_E^2}{2\sigma_{OOP}} + \frac{L_E^2}{2\sigma_{BL}P_E/\kappa_E} + \frac{L_E L_S}{\sigma_{BL}P_S/\kappa_S}\right] + \left[\frac{L_E^2}{D_{BL}P_E/\kappa_E} + \frac{L_S^2}{D_{BL}P_S/\kappa_S} + \frac{L_{AM}^2}{D_{AM}}\right]$$

Capacitive (resistive) terms Diffusive terms

We can estimate τ both before and after extended activation we use known/estimated values of estimate the relevant parameters as given in table S3

[N.B. Here we neglected the time associated with the electrochemical reaction. Here we use the diffusion coefficient in the pores is reduced relative to that in bulk liquid as described by the Bruggeman equation: $D_{Pore} = D_{BL}P/\kappa$, where P is the porosity of the electrode and κ is the tortuosity factor.[31, 32]]

Table S2.

Parameter	Symbol and value	Comment
Volumetric capacity	Q_V	Found using $Q_V = \rho_E Q_{M,Act}(1-M_f)$
Low-rate specific capacity	$Q_{M,Act}$ =1381 mAh/g (before) $Q_{M,Act}$ =2030 mAh/g (after)	From rate fit
Electrode density	ρ_E=988 kg/m^3 (before) ρ_E=702 kg/m^3 (after)	
CNT mass fraction	M_f=0.3	
Electrode thickness	L_E=5.9 μm (before) L_E=5.9 μm (after)	
Electrode conductivity	σ_{OOP}=0.1 S/m	Estimated by comparison with previous results[33]
Bulk electrolyte conductivity	σ_{BL}=0.3 S/m	Typical for LIB electrolytes[34]
Electrode porosity	P_E=0.79 (before) P_E=0.85 (after)	
Electrode tortuosity	κ_E=2 (before) κ_E=1.5 (after)	Before estimated, after reduced by factor mentioned in text
Separator thickness	L_S=20 μm	
Separator porosity	P_S=0.4	Typical
Separator tortuosity	κ_S=3	Typical

Bulk electrolyte diffusivity	2×10^{-10} m^2/s	Middle of the range for common battery electrolytes[35, 36]
Solid state diffusion length	L_{AM}=100 nm (before) L_{AM}=60 nm (after)	Before from platelet thickness, after reduced commensurate with surface area increase
Solid state diffusivity	$D_{AM}=6\times10^{-16}$ m^2/s (before) $D_{AM}=1\times10^{-17}$ m^2/s (after)	Before extracted from ref[37] After value is chosen to give value of τ roughly matching measured value.
Capacitive contribution to τ	**τ_C =87s (before)** **τ_C =140s (after)**	
Diffusive contribution to τ	**τ_D = 32s (before)** **τ_S =376s (after)**	
Total calculated τ	**τ = 119s (before)** **τ = 516s (after)**	**Experimental: τ = 143s (before)** **τ = 578s (after)**

Supplementary references

1. Larcher, D.; Masquelier, C.; Bonnin, D.; Chabre, Y.; Masson, V.; Leriche, J.-M.; Tarascon, J.-M., Effect of Particle Size on Lithium Intercalation into -Fe2O3. *Journal of The Electrochemical Society* **2003,** *150* (Issue 1), A133-A139.
2. Koo, B.; Xiong, H.; Slater, M. D.; Prakapenka, V. B.; Balasubramanian, M.; Podsiadlo, P.; Johnson, C. S.; Rajh, T.; Shevchenko, E. V., Hollow iron oxide nanoparticles for application in lithium ion batteries. *Nano Lett* **2012,** *12* (5), 2429-35.
3. Tang, J.; Zavala Lugo, C. E.; Acuña Guzmán, S. F.; Daniel, G.; Kessler, V. G.; Seisenbaeva, G. A.; Pol, V. G., Pushing the theoretical capacity limits of iron oxide anodes: capacity rise of γ-Fe2O3nanoparticles in lithium-ion batteries. *J. Mater. Chem. A.* **2016,** *4* (46), 18107-18115.
4. Zhou, G.; Wang, D.-W.; Li, F.; Zhang, L.; Li, N.; Wu, Z.-S.; Wen, L.; Lu, G. Q.; Cheng, H.-M., Graphene-Wrapped Fe3O4 Anode Material with Improved Reversible Capacity and Cyclic Stability for Lithium Ion Batteries. *Chem. Mater.* **2010,** *22* (18), 5306-5313.
5. Liu, W.-R.; Wang, J.-H.; Wu, H.-C.; Shieh, D.-T.; Yang, M.-H.; Wu, N.-L., Electrochemical Characterizations on Si and C-Coated Si Particle Electrodes for Lithium-Ion Batteries. *Journal of The Electrochemical Society* **2005,** *152* (9).
6. de Levie, R., On porous electrodes in electrolyte solutions—IV. *Electrochimica Acta* **1964,** *9* (9), 1231-1245.
7. Yu, W.-J.; Zhang, L.; Hou, P.-X.; Li, F.; Liu, C.; Cheng, H.-M., High Reversible Lithium Storage Capacity and Structural Changes of Fe2O3 Nanoparticles Confined inside Carbon Nanotubes. *Advanced Energy Materials* **2016,** *6* (3).
8. Wang, Y.; Guo, J.; Li, L.; Ge, Y.; Li, B.; Zhang, Y.; Shang, Y.; Cao, A., High-loading Fe₂O₃/SWNT composite films for lithium-ion battery applications. *Nanotechnology* **2017,** *28* (34), 345703.
9. Park, C.; Samuel, E.; Joshi, B.; Kim, T.; Aldalbahi, A.; El-Newehy, M.; Yoon, W. Y.; Yoon, S. S., Supersonically sprayed Fe2O3/C/CNT composites for highly stable Li-ion battery anodes. *Chem. Eng. J. (Lausanne)* **2020,** *395*, 125018.
10. Huang, P.; Tao, W.; Wu, H.; Li, X.; Yin, T.; Zhang, Q.; Qi, W.; Gao, G.; Cui, D., N-doped coaxial CNTs@α-Fe2O3@C nanofibers as anode material for high performance lithium ion battery. *Journal of Energy Chemistry* **2018,** *27* (5), 1453-1460.
11. Jiang, X.; Guo, W.; Lu, P.; Song, D.; Guo, A.; Liu, J.; Liang, J.; Hou, F., CNTs@γ-Fe2O3@C composite electrode for high capacity lithium ion storage. *International Journal of Hydrogen Energy* **2018,** *43* (30), 14027-14033.
12. Wang, Z.; Luan, D.; Madhavi, S.; Hu, Y.; Lou, X. W., Assembling carbon-coated α-Fe2O3 hollow nanohorns on the CNT backbone for superior lithium storage capability. *Energy & Environmental Science* **2012,** *5* (1), 5252-5256.
13. Gu, X.; Chen, L.; Liu, S.; Xu, H.; Yang, J.; Qian, Y., Hierarchical core–shell α-Fe2O3@C nanotubes as a high-rate and long-life anode for advanced lithium ion batteries. *Journal of Materials Chemistry A* **2014,** *2* (10), 3439-3444.
14. Chen, M.; Liu, J.; Chao, D.; Wang, J.; Yin, J.; Lin, J.; Jin Fan, H.; Xiang Shen, Z., Porous α-Fe2O3 nanorods supported on carbon nanotubes-graphene foam as superior anode for lithium ion batteries. *Nano Energy* **2014,** *9*, 364-372.
15. Liu, J.; Jiang, J.; Qian, D.; Tan, G.; Peng, S.; Yuan, H.; Luo, D.; Wang, Q.; Liu, Y., Facile assembly of a 3D rGO/MWCNTs/Fe2O3 ternary composite as the anode material for high-performance lithium ion batteries. *RSC Advances* **2013,** *3* (35), 15457-15466.
16. Chou, S.-L.; Wang, J.-Z.; Chen, Z.-X.; Liu, H.-K.; Dou, S.-X., Hollow hematite nanosphere/carbon nanotube composite: mass production and its high-rate lithium storage properties. *Nanotechnology* **2011,** *22* (26), 265401.

17. Cao, Z.; Wei, B., α-Fe2O3/single-walled carbon nanotube hybrid films as high-performance anodes for rechargeable lithium-ion batteries. *Journal of Power Sources* **2013,** *241*, 330-340.
18. Xu, L.; Tian, Y.; Liu, T.; Li, H.; Qiu, J.; Li, S.; Li, H.; Yuan, S.; Zhang, S., α-Fe2O3 nanoplates with superior electrochemical performance for lithium-ion batteries. *Green Energy & Environment* **2018,** *3* (2), 156-162.
19. Gao, G.; Jin, Y.; Zeng, Q.; Wang, D.; Shen, C., Carbon nanotube-wrapped Fe₂O₃ anode with improved performance for lithium-ion batteries. *Beilstein Journal of Nanotechnology* **2017,** *8*, 649-656.
20. Lv, X.; Deng, J.; Wang, B.; Zhong, J.; Sham, T.-K.; Sun, X.; Sun, X., γ-Fe2O3@CNTs Anode Materials for Lithium Ion Batteries Investigated by Electron Energy Loss Spectroscopy. *Chemistry of Materials* **2017,** *29* (8), 3499-3506.
21. Li, Y.; Zhu, C.; Lu, T.; Guo, Z.; Zhang, D.; Ma, J.; Zhu, S., Simple fabrication of a Fe2O3/carbon composite for use in a high-performance lithium ion battery. *Carbon* **2013,** *52*, 565-573.
22. Yu, W.-J.; Hou, P.-X.; Zhang, L.-L.; Li, F.; Liu, C.; Cheng, H.-M., Preparation and electrochemical property of Fe2O3 nanoparticles-filled carbon nanotubes. *Chemical Communications* **2010,** *46* (45), 8576-8578.
23. Yan, N.; Zhou, X.; Li, Y.; Wang, F.; Zhong, H.; Wang, H.; Chen, Q., Fe2O3 Nanoparticles Wrapped in Multi-walled Carbon Nanotubes With Enhanced Lithium Storage Capability. *Scientific Reports* **2013,** *3* (1), 3392.
24. Wu, M.; Chen, J.; Wang, C.; Wang, F.; Yi, B.; Su, W.; Wei, Z.; Liu, S., Facile Synthesis of Fe2O3 Nanobelts/CNTs Composites as High-performance Anode for Lithium-ion Battery. *Electrochimica Acta* **2014,** *132*, 533-537.
25. Ji, L.; Toprakci, O.; Alcoutlabi, M.; Yao, Y.; Li, Y.; Zhang, S.; Guo, B.; Lin, Z.; Zhang, X., α-Fe2O3 Nanoparticle-Loaded Carbon Nanofibers as Stable and High-Capacity Anodes for Rechargeable Lithium-Ion Batteries. *ACS Applied Materials & Interfaces* **2012,** *4* (5), 2672-2679.
26. Cho, J. S.; Hong, Y. J.; Kang, Y. C., Design and Synthesis of Bubble-Nanorod-Structured Fe2O3–Carbon Nanofibers as Advanced Anode Material for Li-Ion Batteries. *ACS Nano* **2015,** *9* (4), 4026-4035.
27. Wu, H. B.; Chen, J. S.; Hng, H. H.; Wen Lou, X., Nanostructured metal oxide-based materials as advanced anodes for lithium-ion batteries. *Nanoscale* **2012,** *4* (8), 2526-2542.
28. Wu, C.; Li, X.; Li, W.; Li, B.; Wang, Y.; Wang, Y.; Xu, M.; Xing, L., Fe2O3 nanorods/carbon nanofibers composite: Preparation and performance as anode of high rate lithium ion battery. *J. Power Sources* **2014,** *251*, 85-91.
29. Zhao, Q.; Liu, J.; Li, X.; Xia, Z.; Zhang, Q.; Zhou, M.; Tian, W.; Wang, M.; Hu, H.; Li, Z.; Wu, W.; Ning, H.; Wu, M., Graphene oxide-induced synthesis of button-shaped amorphous Fe2O3/rGO/CNFs films as flexible anode for high-performance lithium-ion batteries. *Chem. Eng. J. (Lausanne)* **2019,** *369*, 215-222.
30. Horvath, D. V.; Coelho, J.; Tian, R.; Nicolosi, V.; Coleman, J. N., Quantifying the Dependence of Battery Rate Performance on Electrode Thickness. *Acs Applied Energy Materials* **2020,** *3* (10), 10154-10163.
31. Chung, D.-W.; Ebner, M.; Ely, D. R.; Wood, V.; Edwin García, R., Validity of the Bruggeman relation for porous electrodes. *Modelling and Simulation in Materials Science and Engineering* **2013,** *21* (7), 074009.
32. Usseglio-Viretta, F. L. E.; Colclasure, A.; Mistry, A. N.; Claver, K. P. Y.; Pouraghajan, F.; Finegan, D. P.; Heenan, T. M. M.; Abraham, D.; Mukherjee, P. P.; Wheeler, D.; Shearing, P.; Cooper, S. J.; Smith, K., Resolving the Discrepancy in Tortuosity Factor

Estimation for Li-Ion Battery Electrodes through Micro-Macro Modeling and Experiment. *J. Electrochem. Soc.* **2018,** *165* (14), A3403-A3426.
33. Tian, R.; Alcala, N.; O'Neill, S. J. K.; Horvath, D. V.; Coelho, J.; Griffin, A. J.; Zhang, Y.; Nicolosi, V.; O'Dwyer, C.; Coleman, J. N., Quantifying the Effect of Electronic Conductivity on the Rate Performance of Nanocomposite Battery Electrodes. *Acs Applied Energy Materials* **2020,** *3* (3), 2966-2974.
34. Logan, E. R.; Tonita, E. M.; Gering, K. L.; Li, J.; Ma, X.; Beaulieu, L. Y.; Dahn, J. R., A Study of the Physical Properties of Li-Ion Battery Electrolytes Containing Esters. *J. Electrochem. Soc.* **2018,** *165* (2), A21-A30.
35. Ehrl, A.; Landesfeind, J.; Wall, W. A.; Gasteiger, H. A., Determination of Transport Parameters in Liquid Binary Lithium Ion Battery Electrolytes I. Diffusion Coefficient. *J. Electrochem. Soc.* **2017,** *164* (4), A826-A836.
36. Ong, M. T.; Verners, O.; Draeger, E. W.; van Duin, A. C. T.; Lordi, V.; Pask, J. E., Lithium Ion Solvation and Diffusion in Bulk Organic Electrolytes from First-Principles and Classical Reactive Molecular Dynamics. *J. Phys. Chem. B* **2015,** *119* (4), 1535-1545.
37. Penki, T. R.; Shivakumara, S.; Minakshi, M.; Munichandraiah, N., Porous Flower-like α-Fe2O3 Nanostructure: A High Performance Anode Material for Lithium-ion Batteries. *Electrochim. Acta* **2015,** *167*, 330-339.